



HAL
open science

Three-junction monolithic interconnected modules for concentrator photovoltaics

Pierre Albert, Abdelatif Jaouad, Gwenaëlle Hamon, Maïté Volatier, Yannick
Deshayes, Laurent Béchou, Vincent Aimez, Maxime Darnon

► **To cite this version:**

Pierre Albert, Abdelatif Jaouad, Gwenaëlle Hamon, Maïté Volatier, Yannick Deshayes, et al.. Three-junction monolithic interconnected modules for concentrator photovoltaics. *Progress in Photovoltaics*, 2021, 29, pp.603-613. 10.1002/pip.3404 . hal-03174950

HAL Id: hal-03174950

<https://hal.science/hal-03174950v1>







Submitted on 19 Mar 2021

HAL is a multi-disciplinary open access archive for the deposit and dissemination of scientific research documents, whether they are published or not. The documents may come from teaching and research institutions in France or abroad, or from public or private research centers.

L'archive ouverte pluridisciplinaire **HAL**, est destinée au dépôt et à la diffusion de documents scientifiques de niveau recherche, publiés ou non, émanant des établissements d'enseignement et de recherche français ou étrangers, des laboratoires publics ou privés.

RESEARCH ARTICLE

Three-junction monolithic interconnected modules for concentrator photovoltaics

Pierre Albert^{1,2}  | Abdelatif Jaouad¹  | Gwenaëlle Hamon¹ | Maïté Volatier¹ | Yannick Deshayes²  | Laurent Béchou^{1,2}  | Vincent Aimez¹  | Maxime Darnon¹ 

¹Laboratoire Nanotechnologies et Nanosystèmes (LN2)-CNRS IRL-3463, Institut Interdisciplinaire d'Innovation Technologique (3IT), Université de Sherbrooke, Québec, Canada

²Laboratoire de l'Intégration du Matériau au Système (IMS)-CNRS UMR-5218, Université de Bordeaux, Talence, France

Correspondence

Maxime Darnon, Laboratoire Nanotechnologies et Nanosystèmes (LN2)-CNRS IRL-3463, Institut Interdisciplinaire d'Innovation Technologique (3IT), Université de Sherbrooke, 3000 boul. de l'Université, Sherbrooke, J1K 0A5 Québec, Canada.
Email: maxime.darnon@usherbrooke.ca

Funding information

University of Ottawa, Canada; Natural Sciences and Engineering Research Council of Canada, Grant/Award Number: 497981; RENATECH; Université Grenoble Alpes; Chimie Physics and Electronics (CPE); ECL; INSA Lyon; Centre National de la Recherche Scientifique (CNRS); Université de Sherbrooke

Abstract

A core issue in concentrator photovoltaic technology (CPV) is the resistive losses in cells that usually limits the maximum photoconversion efficiency under high concentration. We propose the use of three-junction monolithic interconnected modules (MIM) to mitigate resistive losses by providing high-voltage low-current power. First, we present the fabrication of InGaP/InGaAs/Ge front-contacted microcells with various designs and dimensions. Front-contacted cells are the key enabler for the MIM fabrication and demonstrate good electrical characteristics under one sun, similar to standard-contacted cells. The base front contact size is minimized to limit the unutilized area on the wafer. Second, fabrication techniques for interconnecting cells in MIM are described. Finally, electrical measurements show a record conversion efficiency of 35.1% under 798 suns for the first three-junction MIM reported (17.8% when considering the entire device area). Versatility and further optimization of the devices are discussed to enlarge their field of application.

KEYWORDS

device characterization, front-contacted cells, III-V semiconductors, microcells, microfabrication, monolithic interconnect module, three-junction MIM, three-junction solar cells

1 | INTRODUCTION

Concentrator photovoltaic (CPV) cells and modules under high-power illumination are typically limited in efficiency because of resistive losses. Two major alternative approaches, based on unconventional cell/module assemblies, were proposed to mitigate these losses.

The micro-CPV approach was presented in recent years to mitigate resistive losses among others.¹ In this technology, sub-mm² cells are used to form compact modules. Miniaturizing cells leads to less current to handle—as the photocurrent is proportional to the illuminated area of the cell—and a lower series resistance. Micro-CPV approach requires automated high-speed assembly techniques, such as the ones used for consumer electronics, to maintain the cost

competitiveness. Both micrometre-scale high-efficiency solar cells and cells with both contacts on the rear surface or on the front surface are required and were investigated.^{2–4}

Another approach to limit resistive losses relies on the use of monolithic interconnected modules (MIM). In MIM, subcells are series connected at a wafer level to provide high-voltage low-current mini-modules when the irradiance typically exceeds several tens of watt per square centimeter.⁵ MIM were first introduced with silicon structures in the 1970s, and numerous developments allowed CPV MIM made with GaInP/InGaAs structure to reach a record efficiency of 26.0% under 496 suns.⁶ Whereas methods were proposed for three-junction MIM, no demonstrators were presented yet.⁷ One of the challenges is that both emitter and base contacts must be on the same

This is an open access article under the terms of the Creative Commons Attribution License, which permits use, distribution and reproduction in any medium, provided the original work is properly cited.

© 2021 The Authors. Progress in Photovoltaics: Research and Applications published by John Wiley & Sons Ltd.

side of the wafer, which is not straightforward for the state-of-the-art InGaP/InGaAs/Ge structure. Wiesenfarth et al. proposed front-contacted InGaP/InGaAs/Ge cells that use a back-surface lateral conductive layer to minimize the bulk Ge contribution to resistive losses due to the large dimensions of the cells.⁸ However, these cells were interconnected using the conventional wirebonding technique (i.e., nonmonolithic assembly). The use of Ge-On-Insulator (GOI) wafers and the growth of Ge on semi-insulating GaAs substrates were also proposed to form MIM but not proven experimentally.^{5,9,10}

Combining sub-mm² cells with monolithic interconnection, one can envision to fabricate MIM with dimensions similar to conventional solar cells used for point-focus CPV. In this paper, we first propose fabrication methods to make InGaP/InGaAs/Ge solar cells with both contacts on their front surface. Submillimetre solar cells are then series-connected to one another to form MIM with dimensions in the mm² scale. Devices of various geometries are fabricated and characterized under one sun illumination and high-intensity illumination. A

discussion of the optimization directions for such devices and their applications is finally proposed.

2 | FABRICATION AND CHARACTERIZATION METHODS

2.1 | Front-contacted cell fabrication and designs

a. Front-contacted cells fabrication processes

A commercial quantum dots-enhanced InGaP/InGaAs/Ge structure was used, with the Ge substrate doped at $\sim 10^{17}$ cm⁻³.¹¹ No lateral conduction layer was used. A generic process flow for cell fabrication with standard contacts (base contact is on the back surface of the wafer) was presented in Albert et al.¹² Based on that, Figure 1 shows the major steps used for the fabrication of front-contacted cells.

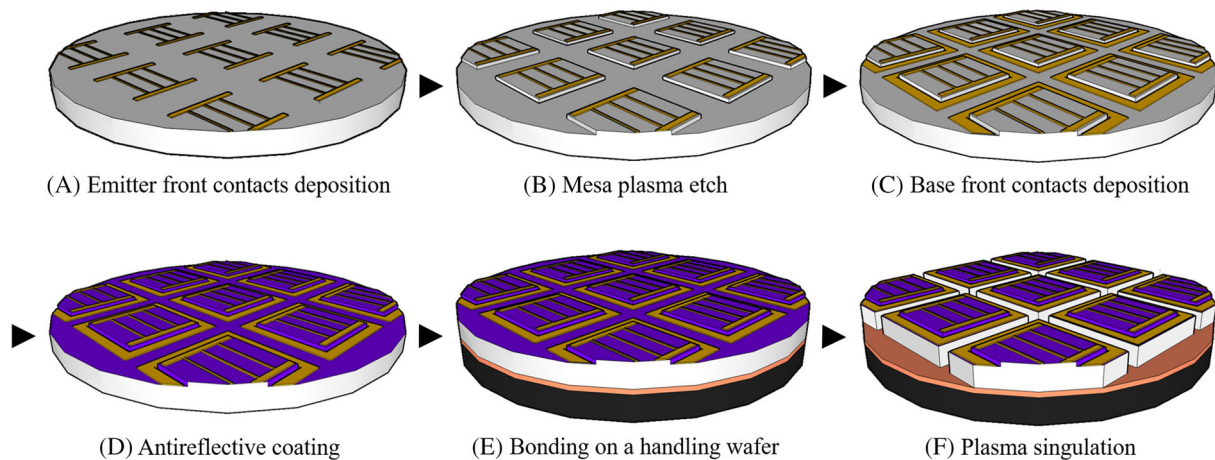


FIGURE 1 Major steps for front-contacted cells fabrication

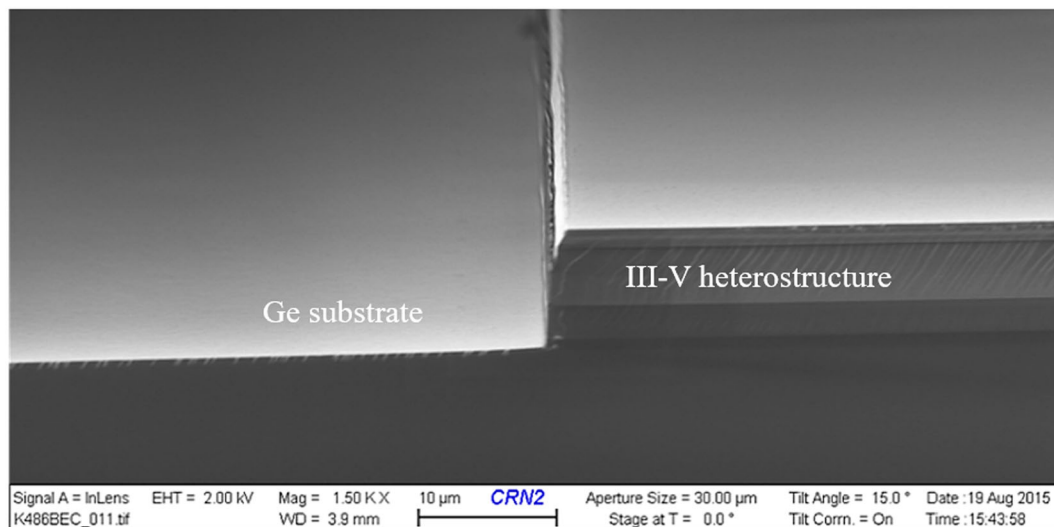


FIGURE 2 Scanning electron microscope tilted view of a plasma-etched cell mesa. The image shows the smoothness of the Ge-substrate surface surrounding the mesa structure. Image: M. de Lafontaine

The first step consists in depositing the emitter contact by evaporating Pd/Ge/Ti/Pd/Al (50 nm/100 nm/50 nm/50 nm/1000 nm) (Figure 1A).¹³ Then, cells are electrically isolated from one another with a SiCl₄/Cl₂/H₂ plasma etch process to form ~10- μ m-high mesas (Figure 1B).^{12,14} The etching step isolates the three subcells (~1 μ m deep in the Ge) and is followed by the contact layer wet etching. The plane surface on the Ge substrate, resulting from the plasma isolation, can be seen on the scanning electron microscope (SEM) in Figure 2. The low topography (lower than the subsequent metallization thickness) is the key enabler for depositing the base contact on the front surface (Figure 1C) using photolithography, instead of the regular backside of the wafer. Ti/Al (50 nm/500 nm) base contacts are evaporated on the etched front surface of the Ge substrate nearby the mesa. To do so, an extra photolithographic step is used, as ohmic contacts were not optimized for both the emitter and the base contacts. No extra conducting layer is added on the back surface. The process is also compatible with the conventional base contact on the wafer backside. In this case, the base contact deposition process on the front side would be skipped and a blank sheet of Ti/Al (50 nm/500 nm) would be evaporated on the wafer rear surface. After the base contact is deposited, an antireflective coating (ARC) that consists in a SiN_xH_y/SiO_xH_y bi-layer (66 nm/69 nm) is deposited by plasma-enhanced chemical vapour deposition (PECVD) and is known to provide cell passivation.¹⁵ As the ARC deposition/passivation is performed at 300°C during approximately 9 min, no additional contact annealing was added. Electrical contacts are revealed by etching the ARC on top of them using CF₄ reactive ion etching (RIE) (Figure 1D). Finally, cells are singulated from the wafer. For this purpose, 500 nm of SiO_x is first deposited on the active wafer rear surface (Ge face) by PECVD before bonding on a handling wafer (Figure 1E). The cell singulation occurs by means of plasma etching through the 170- μ m active wafer (Figure 1F). The etching is performed using a Bosch process that consists in alternating etching steps (13 s, SF₆/O₂) and passivation steps (7 s, C₄F₈) for 45 min (average etch rate is >3.8 μ m/min for 20- μ m-wide trenches).¹⁶ The SiO_x layer acts as an etch-stop layer and can be removed by etching after the cell singulation occurs in case the front-contacted cells are used as stand-alone devices.

b. Front-contacted cells designs

Leveraging the versatility of lithography and plasma etching, we designed and fabricated solar cells with rectangular, circular and

hexagonal active areas. The cell active area dimensions varied between 11.55 and 0.047 mm² (defined as the mesa area to which busbars area is deducted). In rectangular cells, the emitter electrode of square cells is composed of 80- μ m-wide busbars and equally spaced 6- μ m-wide fingers with a pitch of 100 μ m. Unless specified, the base contact has a width w_{BC} of 200 μ m and is surrounding the mesa, further referred as an O-shape contact (contact is adjacent to the four sides of the rectangular mesa). Other base contact designs with I, L and U shapes (contact is adjacent to 1, 2 or 3 sides of the mesa) were also developed. Details on the contact designs are given in the Supporting Information. Photolithographic margins between each level/pattern is $w_{PL} = 10$ μ m (mesa/contact and contact/singulation trench). Cells are diced with singulation trenches of $w_D = 20$ μ m.

Figure 3 shows optical microscope top views of some front-contacted cells (O-shape base contacts) with various designs. In these images, active area varies from 0.044 mm² (circular design) to 0.347 mm² (hexagonal design).

2.2 | MIM fabrication and design

a. MIM fabrication process

The MIM fabrication is performed from the singulated cells, bonded on the handling wafer, as achieved with the processes presented in Section 2.1 (Figure 4A). The first step consists in the electrical isolation between the cells and limits the topography between electrical contacts (Figure 4B). For this purpose, we use an epoxy-based and photosensitive material (SU-8), commonly employed in the microelectronics industry, to completely fill the singulation trenches. Finally, series connection between cells is made using lift-off of evaporated 1- μ m-thick aluminium interconnections (see Figure 4C). A total of seven photolithographic steps are used to complete a MIM with the presented processes. Further optimization could include a one-step metallization as presented in Helmers et al.,⁶ instead of the three steps needed for the contacts and interconnection developed in this work. Figure 5 shows an optical microscope top view (Figure 5A) and a SEM image (Figure 5B) of a 100- μ m-wide interconnection between the emitter contact of the left cell (on one busbar only) and the base contact of the right cell on the top of the SU-8. The singulation trench (20 μ m-wide) can be seen through the SU-8.

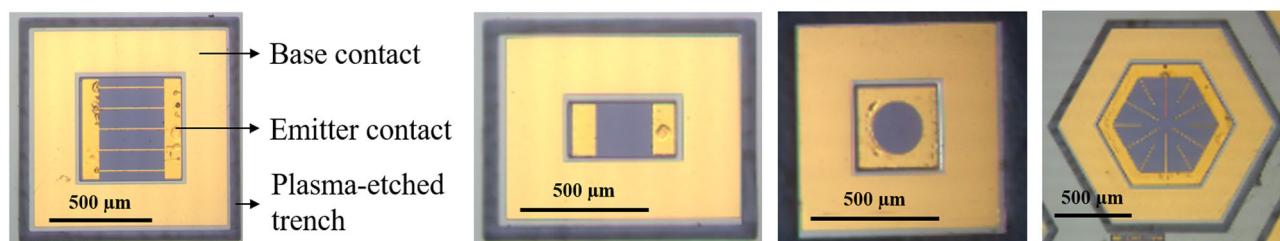


FIGURE 3 Optical microscope view of fabricated front-contacted cells

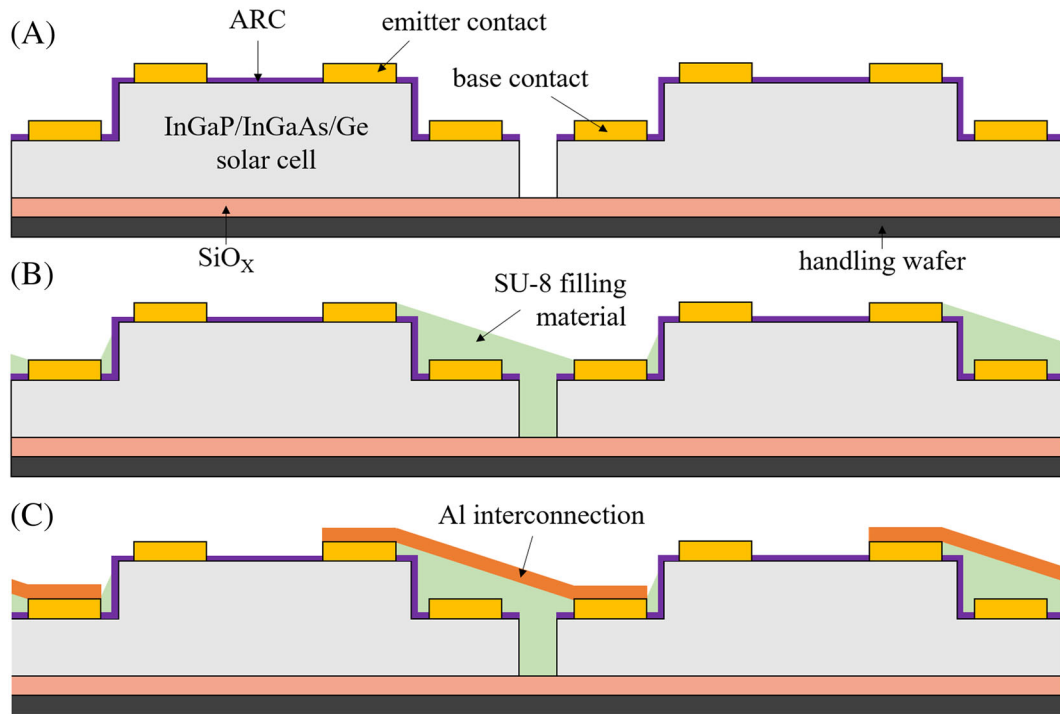


FIGURE 4 Major steps for MIM fabrication (sectional view): (A) two cells are bonded on a handling wafer and singulated, (B) SU-8 material is deposited and engineered to isolate the cells and limit the topography between contacts and (C) Aluminium interconnection is deposited onto SU-8 to achieve the series connection

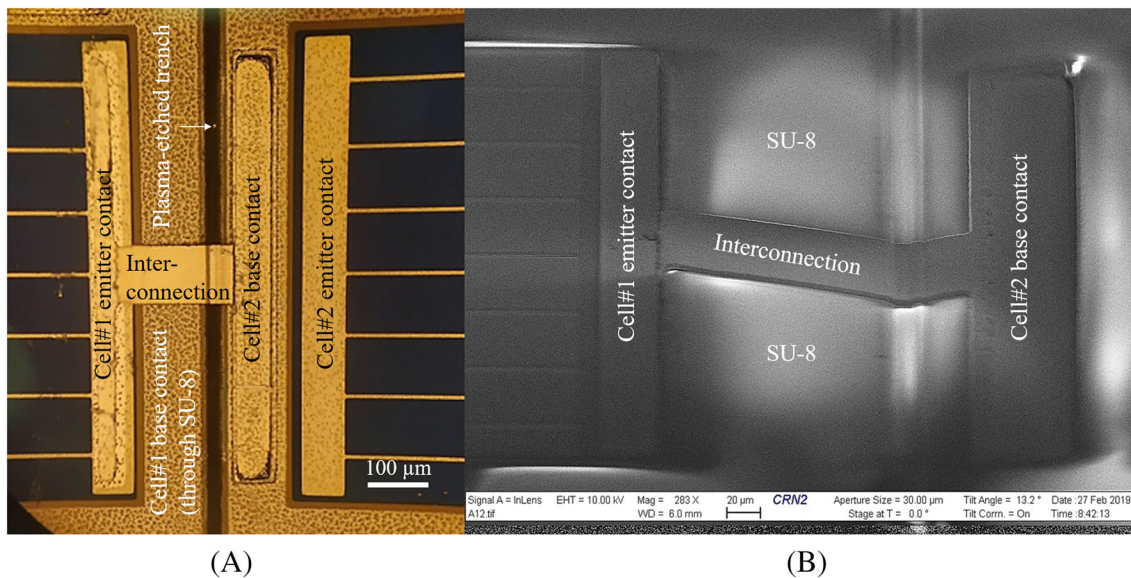


FIGURE 5 (A) Microscope top view of an interconnection between the emitter contact of the left cell and the base contact of the right cell. The singulation trench and base front-contact can be seen through the SU-8 filling material. (B) Scanning electron microscope tilted view of the aluminium interconnection deposited on the SU-8

b. MIM designs

MIM with various shapes (square, circular, hexagonal) with a number of series-connected cells varying from two to nine were designed and fabricated as shown in Figure 6. We chose here designs based on sub- mm^2 cells (between 0.365 and 0.563 mm^2 mesa area per cell in

the images), but the process could be applied on even smaller or larger cells, depending on the targeted application. In the case of square MIM (Figure 6A,B), emitter contacts used the typical design with two busbars. Base contacts consist in U-shape (Figure 6A) or O-shape (Figure 6B) metallization with a width w_{BC} of 100 μm in both cases. Alternative contact designs were proposed for the circular (Figure 6C)

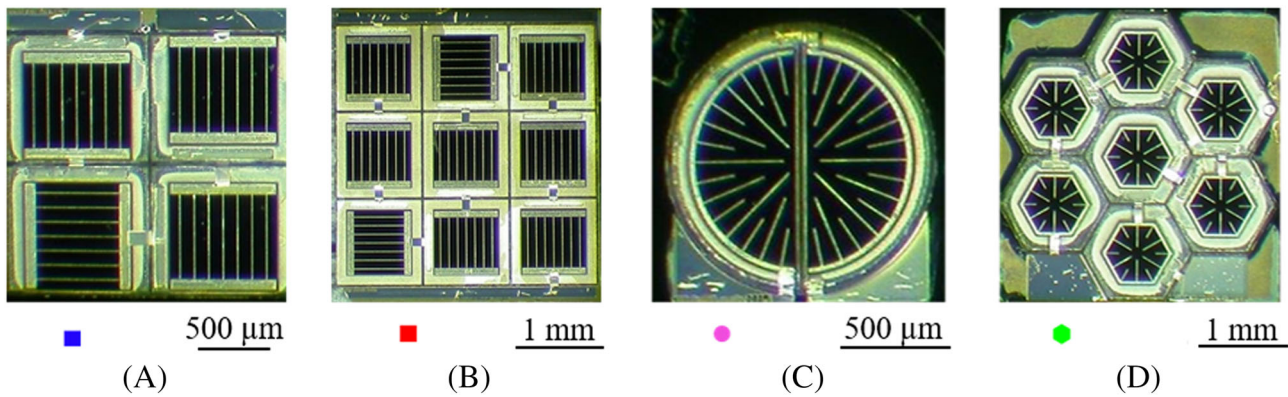
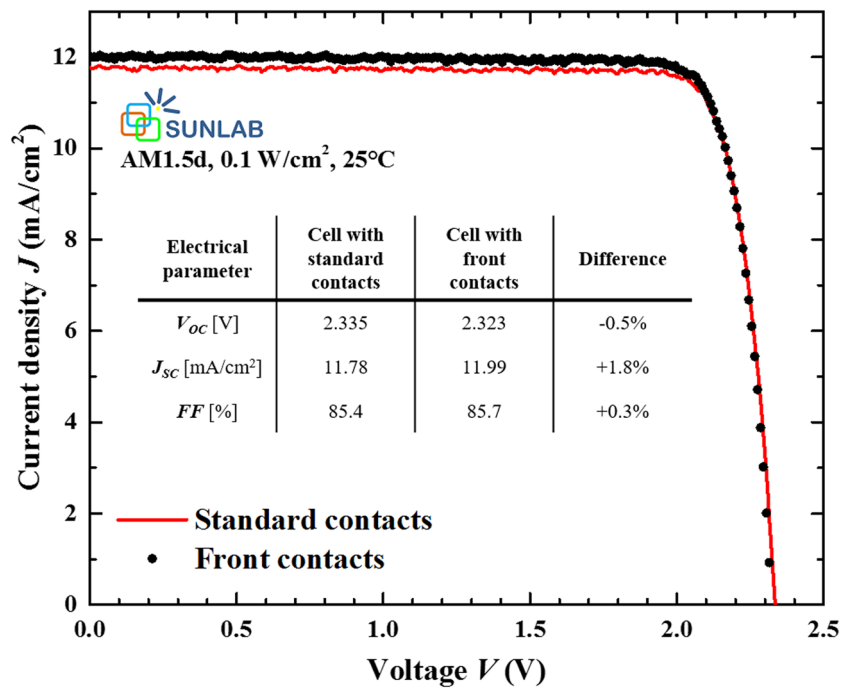


FIGURE 6 Optical microscope top images of fabricated MIMs with (A) a 4-cell square MIM, (B) a 9-cell square MIM, (C) a 2-cell circular MIM and (D) a 7-cell hexagonal MIM

FIGURE 7 One-sun J - V characteristics of square cells (mesa width w_M is 2 mm) with standard (back) or front contacts



and hexagonal (Figure 6D) MIM. Finally, the MIM prototypes have a mesa-to-device area ($\frac{A_{mesa}}{A_{device}}$) comprised between 44.7% (hexagonal MIM; Figure 6D) and 73.0% (circular MIM; Figure 6C). The surface utilization of the MIM is discussed in Section 4.

2.3 | Characterization methods

The electrical characterization of the fabricated cells and MIM are performed under one sun (*AM1.5d* ASTM G173-03 spectrum, 0.1 W/cm^2 , 25°C) and under high illumination. Measurements of the front-contacted cells under one sun and under high-intensity illumination are done at SUNLAB, Ottawa, Canada. The one-sun solar simulator is an Oriol Sol3A-CPV, and the flash tester is an Alpha Omega Power Technologies Gen3. MIM are characterized at SUNLAB under one-sun illumination and at the Fraunhofer Institute for Solar Energy Systems, Freiburg, Germany, for high-intensity light tests with a modified

Technonexan flash tester. Class AAA facilities were used to have a uniform illumination over the small fabricated devices. In order to evaluate semiconductor resistance parameters of the fabricated devices, transfer length measurements (TLM) were also performed, using a 4-probe I - V station. TLM structures consisted in rectangles of $300 \times 120 \mu\text{m}^2$, spaced from 5 to $30 \mu\text{m}$.

3 | RESULTS

3.1 | Front-contacted cells

a. Characterization of front-contacted cells under one-sun illumination

Figure 7 shows the current density/voltage (J - V) characteristics under one sun of square cells with a mesa of 2 mm on a side

($w_M = 2$ mm) with standard contacts (base contact on the entire back surface of the wafer) and front-contacts (200 μm O-shape front base contact). It can be first seen that the J - V characteristics show good results with an open-circuit voltage $V_{OC} > 2.30$ V and a fill factor (FF) $\approx 85.5\%$ as detailed in the inset table. More interestingly, the front-contacted and the standard-contacted cell show similar V_{OC} and FF ($<0.5\%$ variation). The slight increase in J_{SC} (+1.8%) is attributed to light reflections from the base front contact and the probe tips. This result validates the described process for fabricating front-contacted solar cells. These cells can be used as stand-alone devices or as the building blocks for the MIM fabrication.

b. Impact of front base contact on series resistance

The 200- μm -wide O-shape base contacts use a large amount of the expensive wafer compared with the cell size and should be optimized to maximize wafer usage while maintaining a low-enough series resistance to minimize resistive losses. The series resistance of conventional CPV cells results from many parameters (e.g., layers conductivity or electrode geometry). Apart from the bulk germanium resistance and the base contact resistance, one can expect the series resistance of front-contacted cells to be the same as the one of conventional cells.

- Bulk Ge contribution to series resistance

In conventional cells, considering the bulk Ge is uniform, we can evaluate the series resistance $R_{S_Ge}^{back}$ due to the substrate in a back-contacted cell with a square mesa having a width w_M as

$$R_{S_Ge}^{back} = \frac{\rho_{Ge} \times t_{Ge}}{W_M^2}, \quad (1)$$

with ρ_{Ge} the germanium resistivity and t_{Ge} the thickness of the substrate.

In front-contacted cells, the electrons flow laterally in the germanium between their point of entry in the base and the front base contact, which is expected to increase the bulk germanium resistance contribution (longer average distance than the germanium thickness t_{Ge} of 170 μm). Assuming a square mesa with a width w_M , the longest distance electrons have to cross is w_M for I- and L-shape contacts (i.e., with base contact adjacent to one or two sides of the cell; see Supporting Information) or $\frac{w_M}{2}$ for U- and O-shape contacts (i.e., with base contact adjacent to three or four sides of the cell; see Supporting Information).

As a first approximation, one can estimate the series resistance due to bulk Ge in cells with I- or L-shape front contacts $R_{S_Ge}^{front_IL}$ as

$$R_{S_Ge}^{front_IL} < \frac{\rho_{Ge} \times W_M}{W_M \times t_{Ge}}, \quad (2)$$

which is $R_{S_Ge}^{front_IL} < \frac{\rho_{Ge}}{t_{Ge}}$ and in the case of U- and O-shape contacts, $R_{S_Ge}^{front_UO}$ can be estimated as

$$R_{S_Ge}^{front_UO} < \frac{\rho_{Ge} \times \frac{W_M}{2}}{W_M \times t_{Ge}}, \quad (3)$$

which gives $R_{S_Ge}^{front_UO} < \frac{\rho_{Ge}}{2 \times t_{Ge}}$.

Consequently, the increase in bulk Ge contribution to series resistance, due to I- or L-shape front contact, can be expected as

$$\frac{R_{S_Ge}^{front_IL}}{R_{S_Ge}^{back}} < \frac{W_M^2}{t_{Ge}^2}. \quad (4)$$

In the case of U- and O-shape front contacts, the increase of series resistance due to bulk Ge contribution can be estimated as

$$\frac{R_{S_Ge}^{front_UO}}{R_{S_Ge}^{back}} < \frac{W_M^2}{2 \times t_{Ge}^2}. \quad (5)$$

As an example, for cells with $w_M = 500$ μm and $t_{Ge} = 170$ μm , the series resistance due to bulk Ge is predicted to increase by a maximum factor of 8.65 in cells with I- or L-shape contacts and 4.33 in U- or O-shape contacts compared with back-contacted cells.

In conventional cells, bulk germanium contribution to series resistance is considered negligible.¹⁷ Therefore, given the calculations above, it should remain negligible for small dimensions cells. However, it may become significant for cells with a larger w_M . In this case, a lateral conduction layer may be added on the back surface of the Ge substrate (doped at $\sim 10^{17}$ cm^{-3}), as proposed in Wiesenfarth et al.⁸

- Contact contribution to series resistance

In front-contacted cells, the contact area is smaller than the cell surface, which is also anticipated to increase the contact resistance. To evaluate the contact contribution, TLM structures were fabricated on the germanium substrate simultaneously as the solar cells fabrication. A specific contact resistivity ρ_{BC} of 8.02×10^{-5} $\Omega \cdot \text{cm}^2$ and a transfer length L_T of 49.5 μm were found for the used ohmic contact.

In a standard back-contacted cell, one would expect the contact resistance R_{BC} to be

$$R_{BC}^{back} = \frac{\rho_{BC}}{W_M^2}, \quad (6)$$

whereas for a contact width w_C , one would expect a contact resistance R_{BC}^{front} of

$$R_{BC}^{front} = \frac{\rho_{BC}}{W_M \times n_{BC} \times \min(W_{BC}, L_T)}, \quad (7)$$

with $n_{BC} = 1, 2, 3$ or 4 for I-, L-, U- or O-shape front base contacts. The term $\min(w_{BC}, L_T)$ indicates that R_{BC}^{front} is not further lowered by contacts for which w_{BC} is larger than L_T .

Therefore, the increase in contact resistance due front contact can be anticipated as

$$\frac{R_{BC}^{\text{front}}}{R_{BC}^{\text{back}}} = \frac{W_M}{n_{BC} \times \min(W_{BC}, L_T)} \quad (8)$$

As an example, for a cell with $w_M = 500 \mu\text{m}$ and an I-shape contact with $w_{BC} = 10 \mu\text{m}$, the contact resistance is expected to increase by $\frac{R_{BC}^{\text{front}}}{R_{BC}^{\text{back}}} = 50$ compared with a back-contacted cell with the same w_M ($R_{BC}^{\text{front}} = 1.604 \Omega$ and $R_{BC}^{\text{back}} = 32 \text{m}\Omega$ in our case). The same cell with an O-shape contact with $w_{BC} = 49.5 \mu\text{m}$ will result in $\frac{R_{BC}^{\text{front}}}{R_{BC}^{\text{back}}} = 2.5$ ($R_C^{\text{front}} = 82 \text{m}\Omega$ in our case).

However, it was shown in Zimmermann¹⁸ that the contribution of the back contact on the substrate is negligible with respect to the series resistance of the entire three-junction cell. Therefore, depending on the targeted application and given the Equation 8, front contacts may not induce high resistive losses compared to back contacts. The front base contact can be minimized, by preferentially using a width of at least L_T , and an O shape, especially for large cells.

These recommendations have been experimentally verified by measuring the FF under 723 suns of $500\text{-}\mu\text{m}$ -wide cells with various w_{BC} . As shown in Figure 8, the FF as a function of the front base contact width w_{BC} reaches a plateau ($82.5\% < FF < 82.8\%$) when w_{BC} is larger than $50 \mu\text{m}$ (i.e., contact resistance $R_{BC}^{\text{front}} \approx 82 \text{m}\Omega$). This confirms that both bulk Ge and base contact resistance are of minor impact for $w_{BC} \geq 50 \mu\text{m}$ and for $w_M = 500 \mu\text{m}$. However, the FF declines when w_{BC} decreases below $50 \mu\text{m}$, indicating that the contact resistance cannot be neglected anymore when the contact width is smaller than the transfer length L_T . Nonetheless, the FF for $w_{BC} = 10 \mu\text{m}$ (smallest contact width considered here) remains larger than 81% under 723 suns, which indicates that such small contacts could be envisioned for lower concentration applications.

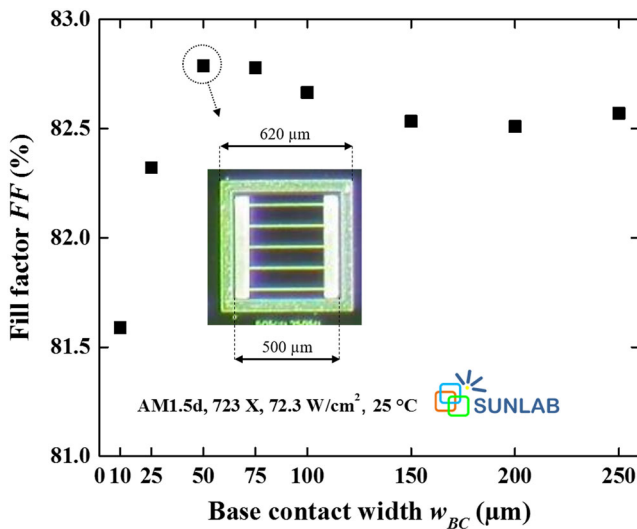


FIGURE 8 Fill factor of square cells (mesa width w_M is $500 \mu\text{m}$) depending on the front base contact width w_{BC} (O-shape) under 723 suns

3.2 | Monolithic interconnected modules

a. Characterization under one-sun illumination

Fabricated MIM were electrically characterized under one sun and under high-intensity light. Figure 9 shows their one-sun current-density-vs-voltage characteristics. In order to validate the MIM performance, the electrical parameters V_{OC} , FF and J_{SC} are compared with those of a single cell.

Considering the interconnections schemes, one can expect

$$V_{OC}^{\text{MIM}} \approx n_{\text{MIM}} \times V_{OC}^{\text{cell}}, \quad (9)$$

where V_{OC}^{MIM} is the open-circuit voltage of the MIM, n_{MIM} is the number of cells that makes the MIM and V_{OC}^{cell} is the open-circuit voltage of a single cell. Because we developed MIM as pseudo-cells, we define the short-circuit current density as the current generated by the whole device divided by its active surface (considered as the total mesa area of all subcells to which busbars area is deducted). Therefore, the short-circuit current density of the MIM J_{SC}^{MIM} is expected to be

$$J_{SC}^{\text{MIM}} = \frac{J_{SC}^{\text{cell}}}{n_{\text{MIM}}}, \quad (10)$$

with J_{SC}^{cell} the short-circuit current density of a single cell and the fill factor of the MIM FF^{MIM} is anticipated as

$$FF^{\text{MIM}} \approx FF^{\text{cell}}, \quad (11)$$

where FF^{cell} is the fill factor of a single cell. This relation stands if the series resistance due to interconnections is negligible. V_{OC} , FF and J_{SC} of the fabricated MIM are summarized in Table 1, in which

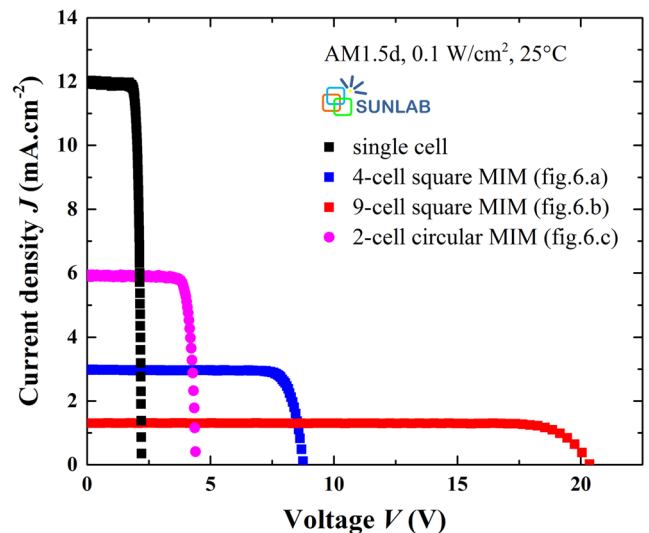
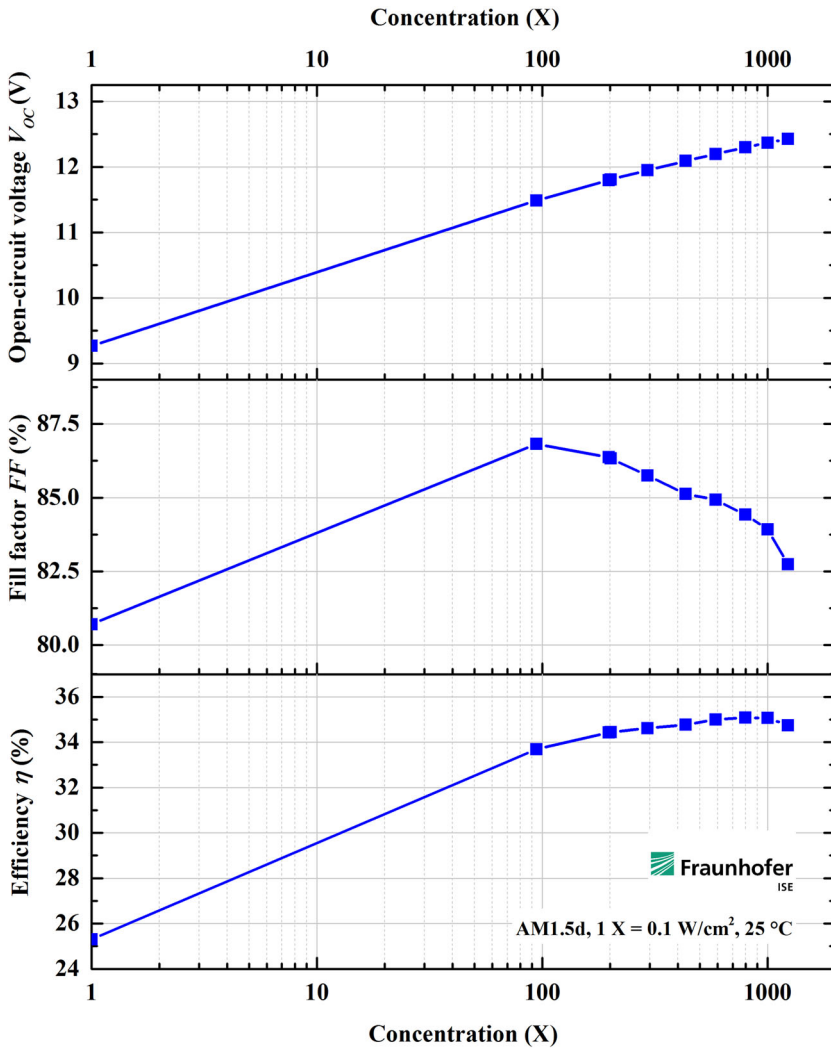


FIGURE 9 J - V characteristics of a single cell and various MIM under a one-sun illumination

TABLE 1 Electrical parameters extracted from the one-sun J - V characteristics of fabricated MIM compared those of a single cell

Electrical parameter AM1.5d spectrum, 0.1 W/cm ² , 25°C	Single cell	4-cell square MIM	9-cell square MIM	2-cell circular MIM
Measured V_{OC} [V] (expected V_{OC} [V], based on the single cell performance)	2.21	8.77 (8.84)	20.36 (19.89)	4.42 (4.42)
Measured J_{SC} [mA/cm ²](expected J_{SC} [mA/cm ²], based on the single cell performance)	12.010	2.975 (3.003)	1.299 (1.334)	5.916 (6.005)
Measured FF [%](expected FF [%], based on the single cell performance)	83.67	84.19 (83.67)	85.12 (83.67)	84.11 (83.67)

**FIGURE 10** Measured open-circuit voltage (top), fill factor (centre) and efficiency (bottom) of a 4-cell square MIM as a function of concentration

they are compared with those of a single cell. The single cell has an active area of 0.489 mm², whereas the measured MIM elementary cells have an active area comprised between 0.458 mm² (4-cell and 9-cell square MIM; Figure 6A,B) and 0.343 mm² (2-cell circular MIM, Figure 6C). The active area of a cell in the MIM is considered as the mesa area to which busbars area and interconnection-induced shading on the mesa were deducted. Figure 9 and Table 1 show that the first prototypes of MIM show remarkable performance with V_{OC} ranging from 4.42 V (2-cell circular MIM; Figure 6C, 2.21 V per cell) to 20.36 V (9-cell-square MIM; Figure 6B, 2.26 V per cell). The variation between measurements

and Equation 9 is comprised between -0.8% and $+2.4\%$ proving the actual interconnection between cells in all cases. Short-circuit current densities (J_{SC}) vary from 5.92 mA/cm² (2-cell circular MIM; Figure 6C) to 1.30 mA/cm² (9-cell square MIM; Figure 6B). Given Equation 10, the measured values of J_{SC} vary from -0.9% to -2.6% compared with the expectations, confirming the good light uniformity and that no cell in the MIM string is limiting. The slight reduction noticed may be attributed to absorption of SU-8 filling material that reach the mesa top. Finally, the measured FF is comprised between 82.4% and 85.1% in all cases, which makes deviations with Equation 11 between $+0.5\%$ and $+1.7\%$. The good electrical

performance of the various-design MIM validates the fabrication of the devices and shows the versatility of the presented processes.

b. Characterization under high-intensity illumination

Figure 10 shows the V_{OC} , FF and the efficiency η of the four-cell square MIM (shown in Figure 6A) as a function of concentration, for which a total active area of 1.829 mm^2 was measured. The V_{OC} has a value as high as 12 V (3 V per cell) under 344 suns (obtained by interpolation) and reaches 12.43 V (3.11 V per cell) under 1231 suns. A maximum efficiency η of 35.1% is reached under 798 suns. The high light intensity at which the peak efficiency is observed is a result of the restrained effect of resistive losses. Indeed, at such concentration ratio, the FF is still as high as 84.4%. It is also notable that η is above 34.7%, with a FF of 82.7% under concentration as high as 1231 suns. This points out that cells interconnection did not induce any noticeable resistive losses and that the MIM can benefit from the high-voltage low-current effect. The maximal efficiency is 17.8% when considering the entire MIM area.

4 | DISCUSSION

4.1 | Surface exploitation of MIM

We have demonstrated the fabrication of front-contacted cells with similar performance to conventional cells. Whereas front-contacted

cells offer opportunities to alternative assembly schemes and MIM development, the base front contact uses semiconductor surface that cannot be used for photoconversion.

We have shown that, using the presented metallization and cells, a base contact width w_{BC} of $49.5 \mu\text{m}$ was necessary for high performance under high concentration. This value corresponds to the transfer length L_T and therefore, as confirmed experimentally in Section 3.1 [b]), a larger contact would not result in a lower series resistance. Only the series resistance due to bulk Ge may affect the largest devices performance, depending on the targeted application and the generated current, and for which a lateral conduction layer may be required, as developed in.⁸ We can easily consider lowering photolithographic margin width to $w_{PL} = 5 \mu\text{m}$ between the structures defined by photolithographic processes and the plasma dicing trench to $w_D = 10 \mu\text{m}$. Therefore, the minimal distance between two adjacent square mesas is $129 \mu\text{m}$ in the case of O-shape base front contacts and $74.5 \mu\text{m}$ in the case of L-shape contacts (see details in the Supporting Information and Figure 11). Thanks to the use of plasma etching as the dicing technique, the lost area between cells is kept low, close to that offered by saw dicing technique in standard-contacted cells (i.e., $\sim 50\text{--}120 \mu\text{m}$).¹⁹

Figure 12 illustrates the $\frac{A_{\text{mesa}}}{A_{\text{device}}}$ of a single front-contacted cell and MIM of 4, 9 and 16 cells with $49.5 \mu\text{m}$ I-shape base contacts, which is the most optimized base contact shape. The A_{mesa} is the mesa area that corresponds to the device area A_{device} minus the lost area due to front base contacts, photolithography margins and dicing trenches in the case of MIM.

As an example, it is shown that a cell with $49.5 \mu\text{m}$ I-shape base contacts for a total area of 10 mm^2 would have a $\frac{A_{\text{mesa}}}{A_{\text{device}}} = 97.6\%$. A

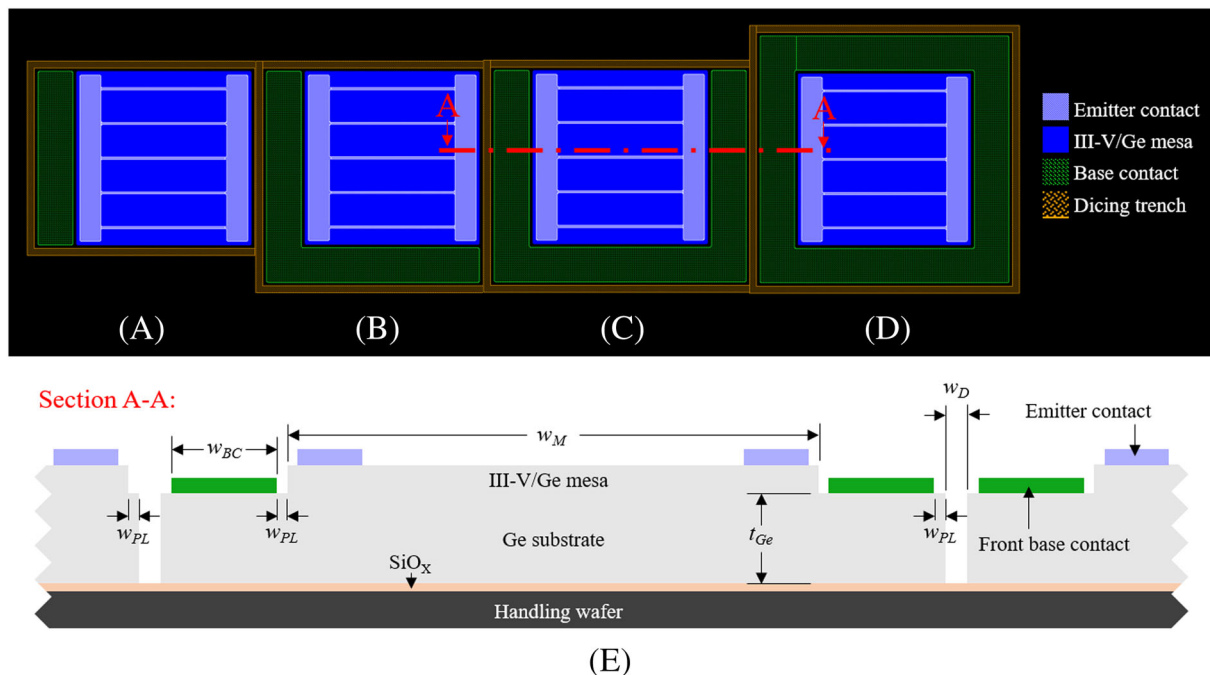


FIGURE 11 Designs of front-contacted cells with a (A) I-, (B) L-, (C) U- and (D) O-shape base contact. A cross section L view along A-A is provided in e. showing adjacent cells with a L- (left), U- (centre) and O-shape (right) base contact

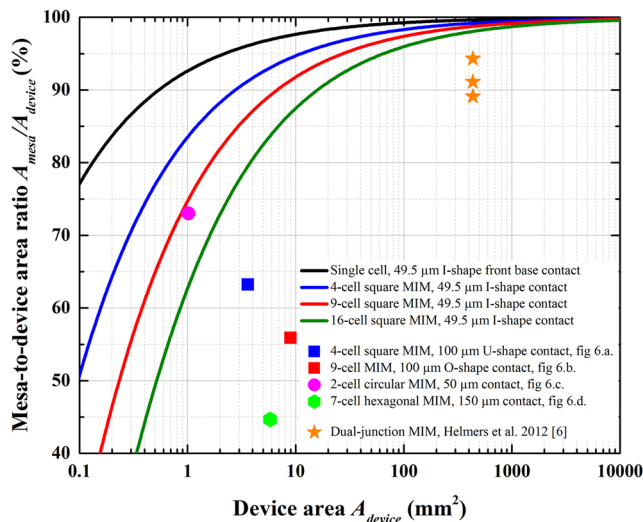


FIGURE 12 Mesa-to-device area ratio $A_{\text{mesa}}/A_{\text{device}}$ as a function of device area A_{device} for a single front-contacted square cell, a 4-cell, a 9-cell and a 16-cell square MIM with I-shape base contacts. The graph also includes the MIM fabricated in this work and the dual-junction MIM demonstrated by Helmers et al.⁶

10-mm² square MIM with 4 cells with I-shape base contact of 49.5 μm would have a $\frac{A_{\text{mesa}}}{A_{\text{device}}}$ of 94.7% and a MIM with the same total area but with 16 cells would have a $\frac{A_{\text{mesa}}}{A_{\text{device}}}$ of 87.5%. Similar trends would be observed for other MIM designs (e.g., hexagonal or circular). Therefore, depending on the targeted module design, a trade-off must be found between the usable active area ($\frac{A_{\text{mesa}}}{A_{\text{device}}}$) and the resistive losses reduction.

Figure 12 also includes the $\frac{A_{\text{mesa}}}{A_{\text{device}}}$ of the different MIM developed in this work. The reported values are $\frac{A_{\text{mesa}}}{A_{\text{device}}} = 63.2\%$ for the 4-cell square MIM (Figure 6A), $\frac{A_{\text{mesa}}}{A_{\text{device}}} = 55.9\%$ for the 9-cell square MIM (Figure 6B), $\frac{A_{\text{mesa}}}{A_{\text{device}}} = 73.0\%$ for the 2-cell circular MIM (Figure 6C) and $\frac{A_{\text{mesa}}}{A_{\text{device}}} = 44.7\%$ for the 7-cell hexagonal MIM (Figure 6D). The $\frac{A_{\text{mesa}}}{A_{\text{device}}}$ was not optimized in these cases.

As a comparison, MIM demonstrated by Helmers et al., for which $89.1\% \leq \frac{A_{\text{mesa}}}{A_{\text{device}}} \leq 94.3\%$ (number of cells in the MIM not communicated) for a $A_{\text{device}} = 4.368 \text{ cm}^2$ device are also given in Figure 12. Such high $\frac{A_{\text{mesa}}}{A_{\text{device}}}$ was obtained thanks to the large area of the entire device. The trends shown on Figure 12 illustrate that $\frac{A_{\text{mesa}}}{A_{\text{device}}} = 94.3\%$ could be reached by the proposed optimized MIM for much lower A_{device} (from 8.6 mm² for a 4-cell MIM to 50.3 mm² for a 16-cell MIM).

It is also important to note that in the case of front-contacted cells or MIM, large busbars on the cell active surface may not be necessary. Indeed, in the case of front-contacted cells, alternative assembly schemes can be proposed (e.g., flip-chip-like technique) instead of wirebonding.^{3,4} In the case of MIM, the cells are interconnected by means of microfabrication techniques, providing very tight features, obtainable by photolithographic processes. One could also envision interconnections to be as large as the cell mesas to further reduce their resistive effect. Moreover, the absence of large busbars reduces

the dark current generation due to the shading, which may be limiting for small-dimension cells.²⁰

4.2 | Applications and limitations

We have shown that MIM are particularly well suited for high-concentration applications, when the high current of conventional cells would reduce the efficiency because of resistive losses.

High concentration MIM is always associated with a reduction of the system acceptance angle. Moreover, due to their series arrangement, MIM are expected to be sensitive to nonuniformity. It is therefore anticipated that MIM integration in point focus concentrator photovoltaic systems would be associated with a secondary optical element. Such element could be co-optimized with the MIM to favour light redistribution outside of the unused area between the MIM subcells, mitigating the negative impact of surface loss, as proposed in Norman et al.²¹ for example. In addition, the process presented in this paper allows the fabrication of densely packed cells, mitigating the cells tilting, typically induced by the shingling technique used for dense-arrays assembly. Finally, MIM could offer the possibility to monolithically integrate by-pass diodes to simplify the complete module assembly, as developed in Loeckenhoff et al.²²

5 | CONCLUSION

We proposed InGaP/InGaAs/Ge cells with both contacts on the front side to allow fabrication of MIM. Plasma etching isolation is the key enabler technology for front-contacted cells fabrication. We demonstrated front-contacted cells with various shapes and dimensions (rectangular, circular and hexagonal and sub-mm² active areas) having the same electrical performance as standard-contacted cells. We found that 50-μm-wide base contacts were necessary for the cells to show good performance under high intensity light illumination (measured at 723 suns). Smaller contacts could be envisioned depending on the targeted application. Front-contacted cells were then monolithically integrated into the first 3J MIM ever fabricated, with various designs and up to 9-series-connected submillimetre-scale cells. Electrical characterization under one-sun illumination shows very good results with a V_{OC} ranging from 4.42 (2-cell MIM) to 20.36 V (9-cell MIM) and J_{SC} values from 5.92 to 1.30 mA/cm². Measurements under high-intensity light have shown a record conversion for a MIM, with 35.1% under 798 suns (17.8% considered the entire device area). This confirms series interconnection between cells did not introduce any noticeable resistive effect. Whereas the mesa-to-device-area ratio of the MIM prototypes was comprised between 45.0% and 73.0%, suggestions to lower lost surface were proposed. Finally, limitations and applications of such devices were discussed for point-focus and dense-array applications, opening path to a future integration in high-concentrator photovoltaics.

ACKNOWLEDGEMENTS

LN2 is a joint International Research Laboratory (Unité Mixte de Recherche IRL 3463) funded and co-operated by Université de Sherbrooke (Canada) and CNRS (France) as well as INSA Lyon, ECL, CPE, Université Grenoble Alpes (UGA) and the French national nanofabrication network RENATECH. The authors acknowledge FRQNT and CNRS for financial support. We acknowledge funding support from the Natural Sciences and Engineering Research Council of Canada, NSERC CREATE 497981. Finally, the authors warmly acknowledge C.E. Valdivia for reviewing this article and K. Hinzer for hosting us at SUNLAB, (University of Ottawa, Canada) to perform electro-optical measurements.

ORCID

Pierre Albert  <https://orcid.org/0000-0003-3383-4960>

Abdelatif Jaouad  <https://orcid.org/0000-0002-1466-7346>

Yannick Deshayes  <https://orcid.org/0000-0002-1328-1724>

Laurent Béchou  <https://orcid.org/0000-0002-0920-3619>

Vincent Aimez  <https://orcid.org/0000-0002-1594-3242>

Maxime Darnon  <https://orcid.org/0000-0002-6188-7157>

REFERENCES

- Dominguez C, Jost N, Askins S, Victoria M, Antón I. A review of the promises and challenges of micro-concentrator photovoltaics. *13th International Conference on Concentrator Photovoltaic Systems*. AIP Publishing LLC; 2017:080003. <https://doi.org/10.1063/1.5001441>
- de Lafontaine M, Darnon M, Colin C, et al. Impact of via hole integration on multijunction solar cells for through cell via contacts and associated passivation treatment. *IEEE Journal of Photovoltaics*. 2017;7(5): 1456-1461. <https://doi.org/10.1109/JPHOTOV.2017.2711423>
- Fidaner O, Suarez FA, Wiemer M, et al. High efficiency micro solar cells integrated with lens array. *Appl Phys Lett*. 2014;104(10):1-5, 103902. <https://doi.org/10.1063/1.4868116>
- Hayashi N, Terauchi M, Aya Y, Kanayama S, Nishitani H, Nakagawa T, Takase M. Thin concentrator photovoltaic module with micro-solar cells which are mounted by self-align method using surface tension of melted solder. *13th International Conference on Concentrator Photovoltaic Systems*. AIP Publishing LLC; 2017:080005. <https://doi.org/10.1063/1.5001443>
- Datas A, Linares PG. Monolithic interconnected modules (MIM) for high irradiance photovoltaic energy conversion: a comprehensive review. *Renew Sustain Energy Rev*. 2017;73:477-495. <https://doi.org/10.1016/j.rser.2017.01.071>
- Helmerts H, Oliva E, Bronner W, Dimroth F, Bett AW. Advanced processing techniques used for the development of dual-junction monolithic interconnected modules, *6th International Conference on Concentrator Photovoltaic Systems*. American Institute of Physics; 2010:39-42. <https://doi.org/10.1063/1.3509227>
- Wanlass MW. High-efficiency, monolithic, multi-bandgap, tandem, photovoltaic energy converters. *US8735202B2*, 2014.
- Wiesenfarth M, Steiner M, Helmerts H, Siefer G, Oliva E, Dimroth F, Shelef G, Polonsky G, Flitsanov Y, Kribus A, Bett AW. Front-side interconnected large area concentrator cells for compact concentrator modules. *8th International Conference on Concentrator Photovoltaic Systems*. American Institute of Physics; 2012:204-207. <https://doi.org/10.1063/1.4753869>
- Akatsu T, Deguet C, Sanchez L, et al. Germanium-on-insulator (GeOI) substrates—a novel engineered substrate for future high performance devices. *Mater Sci Semicond Process*. 2006;9(4-5):444-448. <https://doi.org/10.1016/j.mssp.2006.08.077>
- Cheng YB, Chia CK, Chai Y, Chi DZ. High quality Ge epitaxy on GaAs (100) grown by metal-organic chemical vapor deposition. *Thin Solid Films*. 2012;522:340-344. <https://doi.org/10.1016/j.tsf.2012.08.044>
- Fafard S. Solar cell with epitaxially grown quantum dot material. *U.S. Patent No. 7863516*, 2001. <https://patents.google.com/patent/US7863516B2/ko>
- Albert P, Jaouad A, Hamon G., Volatier M., Valdivia C.E., Deshayes Y., et al. Miniaturization of InGaP/InGaAs/Ge cells for micro-concentrator photovoltaics. Revised manuscript submitted for publication in *Progress in Photovoltaics* on December 24th, 2020.
- Huo P, Rey-Stolle I. Al-based front contacts for HCPV solar cell. *13th International Conference on Concentrator Photovoltaic Systems*. AIP Publishing LLC; 2017:1881, 040004. <https://doi.org/10.1063/1.5001426>
- de Lafontaine M, Pargon E, Petit-Etienne C, et al. Influence of plasma process on III-V/Ge multijunction solar cell via etching. *Solar Energy Materials and Solar Cells*. 2019;195:49-54. <https://doi.org/10.1016/j.solmat.2019.01.048>
- Homier R, Jaouad A, Turala A, et al. Antireflection coating Design for Triple-Junction III-V/Ge high-efficiency solar cells using low absorption PECVD silicon nitride. *IEEE Journal of Photovoltaics*. 2012;2(3): 393-397. <https://doi.org/10.1109/JPHOTOV.2012.2198793>
- Darnon M, de Lafontaine M, Volatier M, et al. Deep germanium etching using time multiplexed plasma etching. *Journal of Vacuum Science & Technology B, Nanotechnology and Microelectronics: Materials, Processing, Measurement, and Phenomena*. 2015;33(6):1-7, 060605. <https://doi.org/10.1116/1.4936112>
- Nishioka K, Takamoto T, Agui T, Kaneiwa M, Uraoka Y, Fuyuki T. Evaluation of InGaP/InGaAs/Ge triple-junction solar cell and optimization of solar cell's structure focusing on series resistance for high-efficiency concentrator photovoltaic systems. *Solar Energy Materials and Solar Cells*. 2006;90(9):1308-1321. <https://doi.org/10.1016/j.solmat.2005.08.003>
- Zimmermann CG. Utilizing lateral current spreading in multijunction solar cells: an alternative approach to detecting mechanical defects. *J Appl Phys*. 2006;100(2):1-8, 023714. <https://doi.org/10.1063/1.2216868>
- Martin D, Sullivan S. Dicing of MEMS devices. In: *Handbook of Silicon-Based MEMS Materials and Technologies*. Elsevier; 2010:671-677.
- Wiesenfarth M, Steiner M, Helmerts H, Bett AW. Voltage losses due to the perimeter and dark area in micro-concentrator solar cells. *Solar Energy Materials and Solar Cells*. 2021;219:1-10, 110791. <https://doi.org/10.1016/j.solmat.2020.110791>
- Norman R, Siskavich B, Fafard S, Béchou L, Ares R, Aimez V, et al. Trough-lens-cone optics with microcell arrays: high efficiency at low cost, *14th International Conference on Concentrator Photovoltaic Systems*. AIP Publishing LLC; 2018:090006. <https://doi.org/10.1063/1.5053544>
- Loeckenhoff R, Dimroth F, Oliva E, et al. Development, characterisation and 1000 suns outdoor tests of GaAs monolithic interconnected module (MIM) receivers. *Progress in Photovoltaics: Research and Applications*. 2008;16(2):101-112. <https://doi.org/10.1002/pip.778>

SUPPORTING INFORMATION

Additional supporting information may be found online in the Supporting Information section at the end of this article.

How to cite this article: Albert P, Jaouad A, Hamon G, et al. Three-junction monolithic interconnected modules for concentrator photovoltaics. *Prog Photovolt Res Appl*. 2021; 1-11. <https://doi.org/10.1002/pip.3404>